Check for updates

Synthesis of CoFe$_2$O$_4$@SiO$_2$–NH$_2$ and its application in adsorption of trace lead†

Yanxia Zeng, [ID] [abcd] Jiliang Xie,[abc] Xin Xiao, [ID] *[abc] Li Chen*[bc] and Xiashi Zhu*[d]

In this work, an amine functionalized CoFe$_2$O$_4$ magnetic nanocomposite material CoFe$_2$O$_4$@SiO$_2$–NH$_2$ was prepared successfully by modifying coated-CoFe$_2$O$_4$@SiO$_2$ magnetic nanoparticles with 3-aminopropyltriethoxysilane (APTES) and became an efficient adsorbent for the separation and analysis of trace lead in water. The CoFe$_2$O$_4$@SiO$_2$–NH$_2$ magnetic nanoparticles were characterized using SEM, TEM, XRD, FTIR, VSM and BET techniques. Then, the adsorption mechanism was preliminarily investigated through ZETA, XPS, and adsorption kinetic experiments. The adsorption process was fitted by pseudo-second-order kinetics and a Langmuir isotherm model. The main adsorption mechanism of CoFe$_2$O$_4$@SiO$_2$–NH$_2$ towards lead ions was the chelation between the amino groups of CoFe$_2$O$_4$@SiO$_2$–NH$_2$ and lead cations, as well as the strong Coulomb interaction between the electron donor atoms O and N in the surface of CoFe$_2$O$_4$@SiO$_2$–NH$_2$ and lead cations. The adsorption capacity is 74.5 mg g^{-1} and the adsorbent can be reused 5 times. Hence, this prepared CoFe$_2$O$_4$@SiO$_2$–NH$_2$ could find potential applications for the removal of trace metal ions in surface water.

1 Introduction

CoFe$_2$O$_4$ is considered to be the most promising permanent magnetic material due to its moderate saturation magnetization strength and good chemical stability.[1] CoFe$_2$O$_4$ is a hard magnetic material belonging to the *Fd3m* space group which has an anti-spinel cubic structure with the molecular formula $(M_{1-\delta}^{2+}Fe_{\delta}^{3+})[M_{\delta}^{2+}Fe_{2-\delta}^{3+}]O_4$, with the cations in parentheses occupying tetrahedral sites and those in square brackets occupying octahedral sites respectively. The degree of inversion delta (δ) depends on the synthesis method and heat treatment and is 0 for normal spinel ferrite and 1 for anti-spinel ferrite.[2] Although CoFe$_2$O$_4$ has been reported to have some extraction ability,[3] simple CoFe$_2$O$_4$ nanomaterials are not adequate in this respect due to their agglomeration, unstable nature, and few surface active groups. Functionalized modification of the surface of CoFe$_2$O$_4$-based core–shell carriers can further improve their extraction ability.

[a] Jiangsu Key Laboratory of Marine Bioresources and Environment, Jiangsu Ocean University, 59 Cangwu Road, Haizhou, Lianyungang 222005, China. E-mail: xiaoxin@njust.edu.cn

[b] Co-Innovation Center of Jiangsu Marine Bio-industry Technology, Jiangsu Ocean University, 59 Cangwu Road, Haizhou, Lianyungang 222005, China. E-mail: chenli@jou.edu.cn

[c] Jiangsu Institute of Marine Resources Development, 59 Cangwu Road, Haizhou, Lianyungang 222005, China

[d] School of Chemistry and Chemical Engineering, Yangzhou University, Yangzhou City, Jiangsu Province 225009, China

† Electronic supplementary information (ESI) available. See DOI: https://doi.org/10.1039/d3ra06091h

SiO$_2$ is widely used in the fields of catalysis, adsorption, and biomedicine because of its cheap availability, stable chemical properties, non-toxicity, and large specific surface area. SiO$_2$ has silicon hydroxyl groups on its surface, which is favorable for the preparation of core–shell shaped composites.[4] The SiO$_2$ layer not only prevents oxidation and aggregation in solution, but also obtains high chemical inertness in almost the whole pH range, excellent biocompatibility, feasibility and diversity of surface modifications, and is easy to be modified to obtain good magnetic response and new properties.[5] Some literature reports suggest that further functionalization of CoFe$_2$O$_4$@SiO$_2$ nanoparticles is more advantageous and effective in removing various metal ions from aqueous solutions.[6,7] Combining the high adsorption capacity of nanoparticles and the easy separation characteristics of CoFe$_2$O$_4$ magnetic cores, the preparation of magnetic nanocomposites or further surface modification with specific ligands has been proved to be an effective method to obtain selective, rapid, simple and high adsorption capacity extractants for trace metals extraction.[8] SiO$_2$ coating on CoFe$_2$O$_4$ magnetic cores can increase the stability, dispersion and active site of pure CoFe$_2$O$_4$ nanoparticles in solution.[9] Some literature reports suggest that further functionalization of CoFe$_2$O$_4$@SiO$_2$ nanoparticles is more advantageous and effective in removing various metal ions from aqueous solutions.[5,10]

This paper establishes a new method for the separation of trace amounts of lead ions in water using magnetic solid-phase extraction ICP-OES, which is based on the preparation of magnetic nanocomposites CoFe$_2$O$_4$@SiO$_2$–NH$_2$ as an

extractant. The particles were characterized by SEM, TEM, EDS, XRD, FRIR, TGA, VSM, and BET experiments, the factors that affect the extraction and elution of trace lead ions were optimized, and this method was applied to the actual determination of lead content in water samples.

2 Materials and experiment methods

2.1 Materials

Ethylene glycol (EG), ethanol absolute, ferric chloride ($FeCl_3 \cdot 6H_2O$), cobalt chloride ($CoCl_2 \cdot 6H_2O$), anhydrous sodium acetate (CH_3COONa), polyethylene glycol (molecular weight 4000), and ammonia water (25% NH_3 H_2O) were purchased from Macklin Reagent (Shanghai, China). All other reagents were purchased from Sinopharm Chemical Reagent Co., Ltd (Shanghai, China) and were of analytical grade or better unless otherwise stated. Ultrapure water (Millipore, Milli-Q) was used for reagent water throughout the studies.

2.2 Preparation of $CoFe_2O_4$@SiO_2 MNPs

$CoFe_2O_4$ MNPs were synthesized using hydrothermal technology.[11] Typically, $FeCl_3 \cdot 6H_2O$ (5.405 g) and $CoCl_2 \cdot 6H_2O$ (2.375 g) were dissolved in ethylene glycol (90 mL), and stirred at 323 K for 30 min. Then, a certain amount of CH_3-COONa (7.335 g) and polyethylene glycol (2.0 g) were added into the mixture with magnetic stirring for 30 min. Subsequently, the suspension was moved into a Teflon reactor (150 mL) and placed in an oven at 473 K for 16 h without stirring. After that, magnetic decanting was used to wash with ethanol three to four times, the above solution was then further washed with ultrapure water until the pH was close to neutral. The obtained $CoFe_2O_4$ materials were dried and bagged for use.

$CoFe_2O_4$@SiO_2 nanoparticles were prepared by using an improved Stöber method.[12] $CoFe_2O_4$ magnetic nanoparticles (0.100 g) were dissolved in ethanol and deionized water by sonication for 30 min, and then a certain amount of cetyltrimethylammonium bromide (CTAB) and 1.00 mL tetraethyl silicate (TEOS) were added sequentially in a weakly alkaline environment. The mixture was reacted for 12 h at 40 °C under continuous stirring. The resulting product was collected by an external magnetic field and rinsed with deionized water and ethanol six times thoroughly. The

resulting product was then dried in vacuum to obtain $CoFe_2O_4$@SiO_2 MNPs.

2.3 Preparation of $CoFe_2O_4$@SiO_2–NH_2 MNPs

The particle was prepared according to the reference literature with slight modifications.[13] The experimental steps are as follows: $CoFe_2O_4$@SiO_2 MNPs (2.0 g) were dispersed into 150 mL of *ortho* xylene and stirred at 50 °C for 1 h. Then, 8 mL of 3-aminopropyltriethoxysilane (APTES, 99.0%) was dropped into the suspension through a constant pressure titration funnel and the mixture was mechanically stirred in an oil bath at 100 °C for 24 h. The reaction products were separated using permanent magnets, washed with water and ethanol to neutral, vacuum dried at 80 °C for 12 h, and then bagged to obtain $CoFe_2O_4$@SiO_2–NH_2 product. The synthesis procedure was illustrated in Fig. 1.

2.4 Procedure for extraction

The general extraction procedure was illustrated in Fig. 2. A series Pb^{2+} standard solution or sample solution, buffer solution (pH = 8.00) solution, and 10 mg $CoFe_2O_4$@SiO_2–NH_2 MNPs were sequentially added to a centrifuge tube and brought to a constant volume of 200.00 mL. Subsequently, the solution in the tube was shaken at constant temperature and left to stand at 50 °C for 30 min. Then use Nd-Fe-B permanent magnetic material to collect $CoFe_2O_4$@SiO_2–NH_2 MNPs containing Pb^{2+} extraction solution, stewing it for about 10 min until the suspension becomes clear, and then use pipette to absorb the supernatant. The MNPs were ultrasonically eluted by 8.0 mL 1 mol L^{-1} hydrochloric acid for 2.5 min. The eluted solution was collected and brought up to volume, and the target analyte was detected with ICP-OES. The entire process takes about 43 min in duration.

2.5 Sample preparation

The water samples were collected from several reservoirs and springs in Lianyungang City, China. The pre-treatment steps of the sample are carried out according to the Chinese National Standard method.[14] Approximately 50.0 mL of the lake water samples were filtered through a 0.45 μm membrane to remove suspended particles before analysis. The samples were stored at −4 °C in a refrigerator. The location of sampling points is shown in Fig. 3.
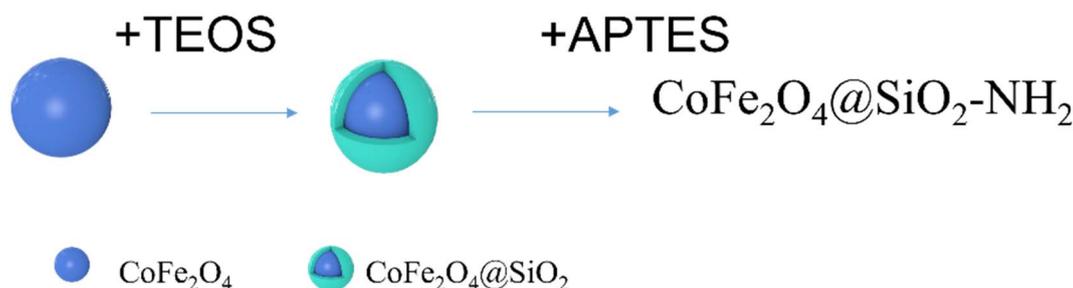

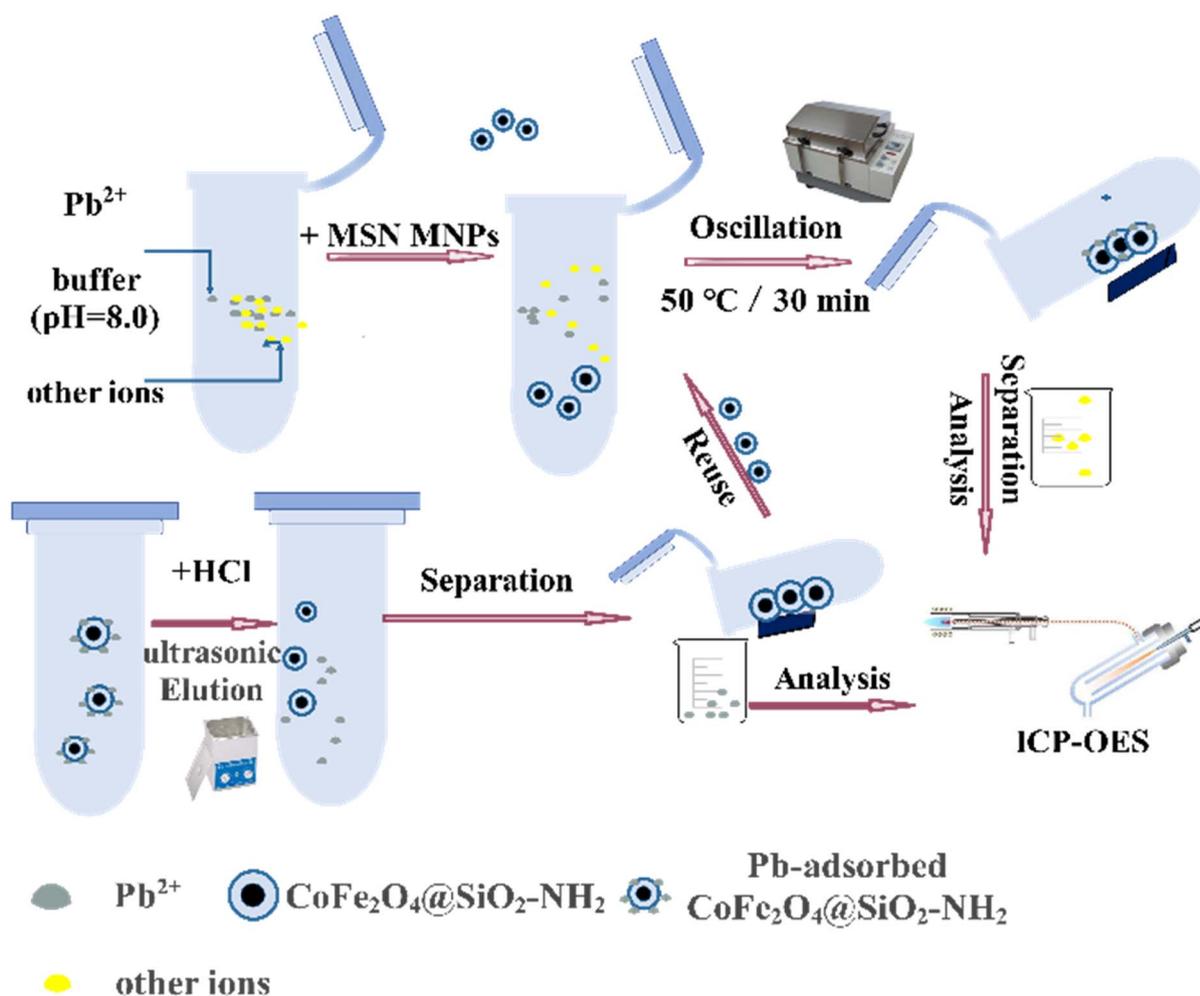**Fig. 1** The synthesis procedure of $CoFe_2O_4$@SiO_2–NH_2.

Fig. 2 Schematic process of the MSPE procedure for detecting Pb^{2+} content using $CoFe_2O_4@SiO_2–NH_2$ as the absorbent.

3 Results and discussion

3.1 Characterization of the MNPs

3.1.1 SEM and TEM analysis. SEM images show that the prepared $CoFe_2O_4$, $CoFe_2O_4@SiO_2$, $CoFe_2O_4@SiO_2–NH_2$ and $CoFe_2O_4@SiO_2–NH_2$ after adsorption are monodisperse (Fig. 4). It can be seen that $CoFe_2O_4$ nanoparticles are spherical, while the surface of the particles is rough and there is obvious agglomeration (Fig. 4a). SiO_2 coated nanoparticles are spherical, monodisperse, smooth and slightly agglomerated (Fig. 4b). In addition, the aminated nanoparticles are still spherical, and the spherical morphology of the nanoparticles did not change significantly after the adsorption of lead ions but the agglomeration increased (Fig. 4d). The typical core–shell structure of $CoFe_2O_4@SiO_2$ is observed in TEM samples with an black spherical inner structure caused by the original $CoFe_2O_4$ magnetic particles and an light black spherical outer layer due to silica coating (Fig. 5b). TEM of $CoFe_2O_4@SiO_2–NH_2$ after the adsorption of lead ions shows no significant change after amino functionalization and the adsorption (Fig. 5d), and the prepared $CoFe_2O_4@SiO_2–NH_2$ nanoparticles have a relatively dense typical core–shell structure, with nano sizes ranging from 50 to 60 nm (Fig. 5c). SEM and TEM images indicated that the aminated materials have been successfully prepared and there is no significant change in the morphology and nanostructure after the adsorption of lead ions.

3.1.2 EDX analysis. The elemental composition of the $CoFe_2O_4$, $CoFe_2O_4@SiO_2$ and $CoFe_2O_4@SiO_2–NH_2$ nanoparticles were estimated using an energy dispersive spectrometer (EDX JSX-1000S) detector (Fig. 6). The results of the energy spectrum prove that $CoFe_2O_4$ contains three elements Co, Fe, and O, with a Co/Fe atomic number ratio of 1 : 2 (Fig. 6A). $CoFe_2O_4@SiO_2$ contains Co, Fe, O, and Si, with a Si atomic number content of 20% (Fig. 6B). The elements identified in the composite structure of the prepared $CoFe_2O_4@SiO_2–NH_2$ nanoparticles were C, N, O, Fe, Co and Si, with atomic percentages of 26.8, 2.47, 24.2, 13.2, 6.28 and 27.3%, respectively. $CoFe_2O_4@SiO_2–NH_2$ contains element N, indicating that NH_2^- has been successfully loaded onto $CoFe_2O_4@SiO_2$ nanoparticles (Fig. 6C).

3.1.3 XRD analysis. Phase investigation of the crystallized product was performed by X-ray powder diffraction (XRD X'Pert Pro). Analysis for $CoFe_2O_4$ nanoparticles, SiO_2, and amino coated nanoparticles (Fig. 7). The XRD results indicate that
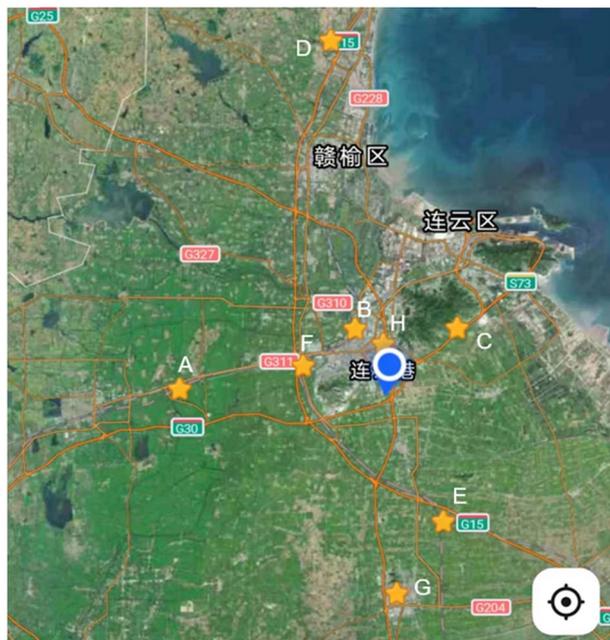
Fig. 3 Location of each water sample sampling point.

$CoFe_2O_4$ exhibits typical diffraction peaks of 18.13°, 30.27°, 35.74°, 43.47°, 53.89°, 57.17°, 62.73°, which are attributed to the [111], [220], [311], [400], [422], [511], and [440] crystal planes of $CoFe_2O_4$, respectively.[4] A typical $CoFe_2O_4$ crystal phase was prepared (Fig. 7a), and the $CoFe_2O_4$ crystal phase has a cubic spinel structure (JCPDS card: 22-1086).[15] All the diffraction peaks of $CoFe_2O_4@SiO_2$ and $CoFe_2O_4@SiO_2–NH_2$ are the same as $CoFe_2O_4$, and there are no diffraction peaks that match that of SiO_2, indicating that the loaded SiO_2 is amorphous and does not change the crystal form of $CoFe_2O_4$. The wide peak at 23° shows the amorphous silica structure (Fig. 7b and c). After amino functionalization loading, the intensity of the diffraction peak changed, nevertheless the peak position was the same as $CoFe_2O_4$, indicating that the crystal form of $CoFe_2O_4$ did not change after amino functionalization. And the peak positions didn't change either, indicating that the crystal morphology of amino functional material did not change after the adsorption of lead ions (Fig. 7d).[16]

3.1.4 Characterization by FTIR. The surface properties of the sample after silanization and amino functionalization before and after adsorption were qualitatively evaluated using infrared spectroscopy (FTIR Tensor 27), and the results are shown in Fig. 8. From the comparison of $CoFe_2O_4$, $CoFe_2O_4@SiO_2$, $CoFe_2O_4@SiO_2–NH_2$ and $CoFe_2O_4@SiO_2–NH_2$ after adsorption spectra, it can be concluded that all four materials have typical Fe–O bond characteristic peaks at 582 cm^{-1}, and the intensity of these peaks gradually weakens with the increase of silicon shell thickness. The peak at 582 cm^{-1} was assigned to Co–O–Fe stretching vibration and the strong peaks at 963 cm^{-1} and 1084 cm^{-1} correspond to
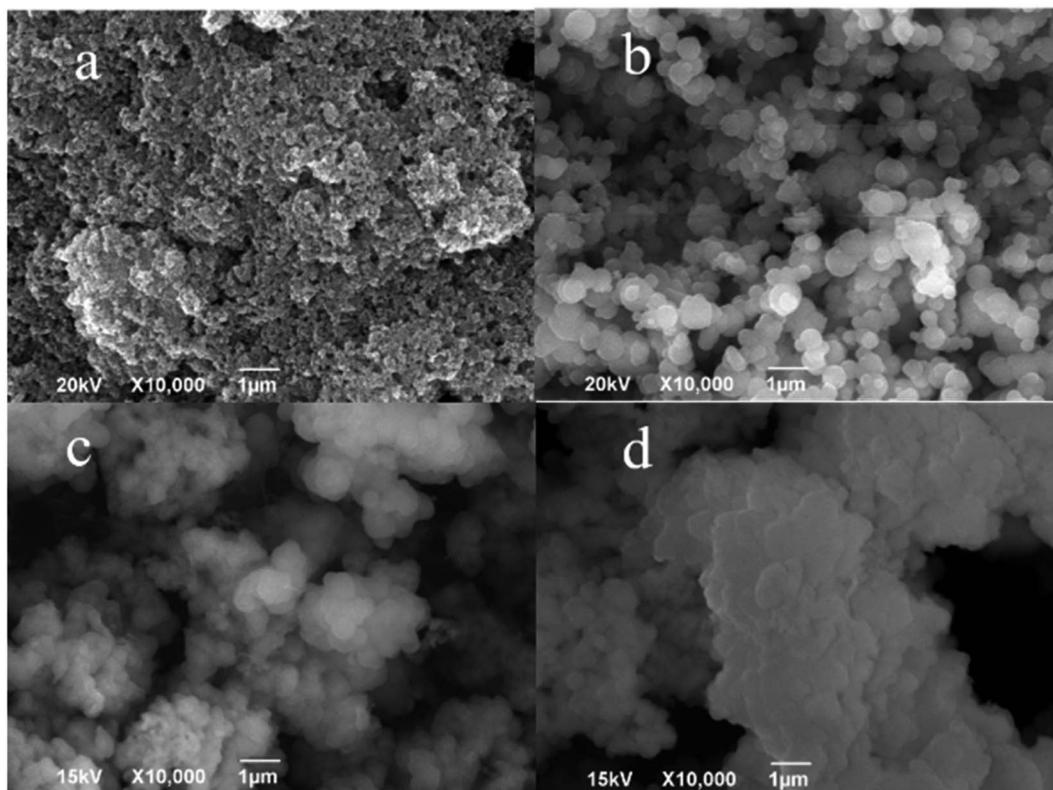

Fig. 4 SEM images of (a) $CoFe_2O_4$, (b) $CoFe_2O_4@SiO_2$, (c) $CoFe_2O_4@SiO_2–NH_2$ and (d) $CoFe_2O_4@SiO_2–NH_2$ nanoparticles after adsorption of lead ions.
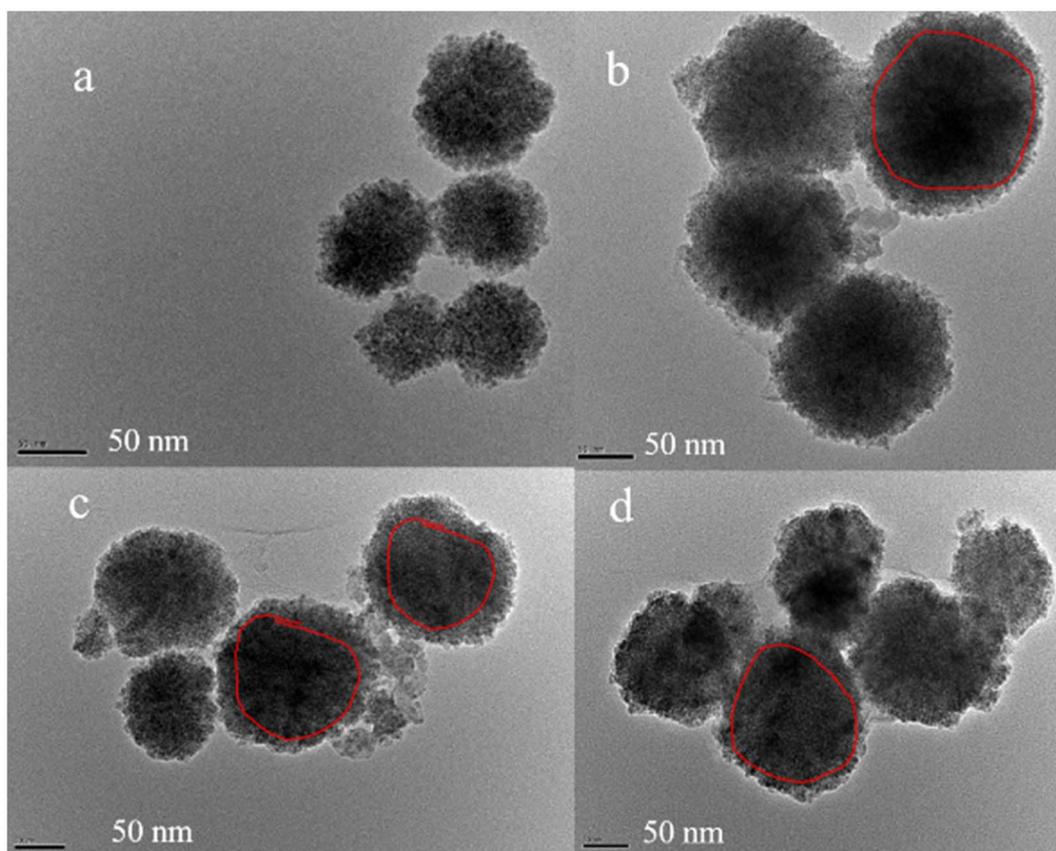
Fig. 5 TEM micrographs of (a) $CoFe_2O_4$, (b) $CoFe_2O_4@SiO_2$, (c) $CoFe_2O_4@SiO_2-NH_2$ before adsorption and (d) $CoFe_2O_4@SiO_2-NH_2$ after adsorption.
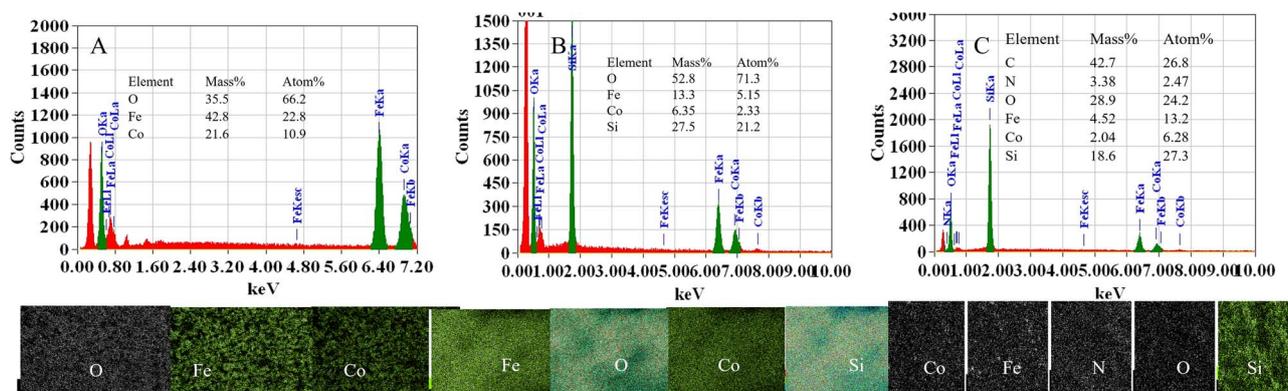
Fig. 6 EDS of (A) $CoFe_2O_4$, (B) $CoFe_2O_4@SiO_2$ and (C) $CoFe_2O_4@SiO_2-NH_2$.

the Si–O–H and Si–O–Si stretching vibration, respectively, which indicate that SiO_2 was successfully loaded on the surface of $CoFe_2O_4$.[17] Compared with pure APTES, the widening of shoulder width at 963 cm^{-1} may be related to the contribution of Si–O–Fe vibration.[18] In $CoFe_2O_4@SiO_2$ spectra curve, the peaks at 3425–3440 and 1629–1632 cm^{-1} correspond to the O–H stretching and bending vibrations of silanol groups with –OH groups and adsorbed water molecules. There are bending vibrations of O–Si–O groups at 958 and

797 cm^{-1} on the $CoFe_2O_4@SiO_2$ nanoparticles, and 469 cm^{-1} is a characteristic peak of Si–O–H, which confirms the formation of silica shell and indicates that the prepared material is successfully covered by silica shell.[19] For $CoFe_2O_4@SiO_2-NH_2$, the new extraction peak at 588 cm^{-1} also corresponds to O–H–N stretching vibration and the new peak around 1209 cm^{-1} in $CoFe_2O_4@SiO_2-NH_2$ is attributed to deformation vibration of –NH groups. And characteristic vibrations around 2930 and 2910 cm^{-1} are related to the
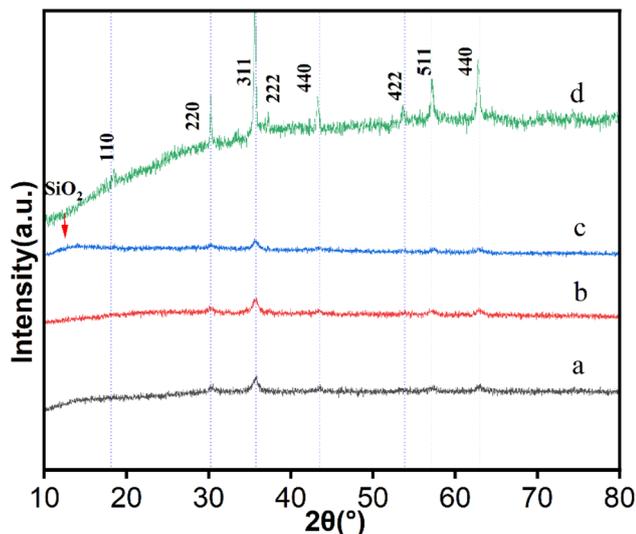
Fig. 7 XRD patterns of (a) $CoFe_2O_4$, (b) $CoFe_2O_4@SiO_2$, (c) $CoFe_2O_4@SiO_2-NH_2$ and (d) $CoFe_2O_4@SiO_2-NH_2$ after lead adsorption.
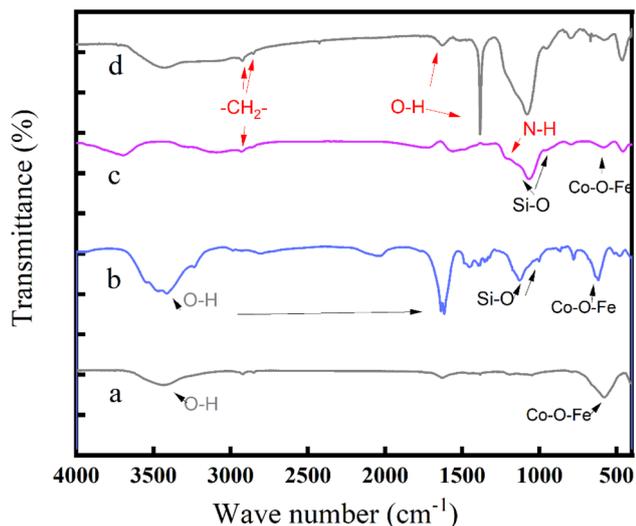
Fig. 8 FTIR spectra of (a) $CoFe_2O_4$, (b) $CoFe_2O_4@SiO_2$, (c) $CoFe_2O_4@SiO_2-NH_2$ and (d) $Pb-CoFe_2O_4@SiO_2-NH_2$.

stretching of asymmetric and symmetric vibrations of $-CH_2-$ group of APTES, while 1620 and 1384 cm^{-1} are due to the characteristic vibrations and stretching of $-O-H$ groups from hydrolysis of APTES (Fig. 8c and d). In addition, the typical absorption band of C–N at 1370 cm^{-1} cannot be observed in the spectrum of Pb(II) with the same intensity, suggesting that Pb(II) have been extracted on $CoFe_2O_4@SiO_2-NH_2$ surface through interaction with valence electrons of amino functionalized groups (Fig. 8d).[9] These results indicate that the silica shell has been successfully amino-functionalized and that lead ions can be successfully extracted by the prepared aminated material.

3.1.5 Thermogravimetric analysis. Thermogravimetric analysis (TGA) revealed the different quality loss processes of

$CoFe_2O_4@SiO_2$ as well as that of $CoFe_2O_4@SiO_2-NH_2$ (Fig. 9). The experimental results show that from 35 to 200 °C, there is a small amount of mass loss (1.56 to 4.12%) of $CoFe_2O_4$, $CoFe_2O_4@SiO_2$ and $CoFe_2O_4@SiO_2-NH_2$, which was attributed to water and residual solvents on the material surface. The second phase of $CoFe_2O_4@SiO_2$ and $CoFe_2O_4@SiO_2-NH_2$ occurs at 200–880 °C, and the weight loss accelerates at 270.9 and 344.8 °C, with weight loss rates of 23.09% and 23.63%, respectively. The maximum mass loss of $CoFe_2O_4@SiO_2$ is within the range of 196–305 °C, with a mass loss of 11.8%, mainly due to the combustion and decomposition of TEOS or APTES molecules. There is little loss of weight in the TGA curves above 650 °C, showing that the aminated $CoFe_2O_4@SiO_2$ MNPs are stable in this temperature range.[15] The experiment results suggest that the aminated experimental material was successfully prepared and was thermally stable.

3.1.6 Magnetic characterization. The maximum saturation magnetization of $CoFe_2O_4$ is measured by vibrating sample magnetometer (VSM STA449F3). The maximum saturation magnetization of $CoFe_2O_4$, $CoFe_2O_4@SiO_2$ and $CoFe_2O_4@SiO_2-NH_2$ MNPs is 59.3, 39.1 and 24.2 emu g^{-1} respectively (Fig. 10). The decrease of maximum saturation magnetization of $CoFe_2O_4@SiO_2-NH_2$ is caused by non-magnetic SiO_2 and amino loading. The hysteresis loops (VSMs) of three MNPs are shown in Fig. 8. The results show that when there are magnetite particles in the magnetic core, the three MNPs both show super-paramagnetism. Although the saturation magnetization of $CoFe_2O_4$ core decreases after coating silica gel and amino group, the saturation magnetization of 24.2 emu g^{-1} is still enough for magnetic separation with magnets.[30] Therefore, the prepared $CoFe_2O_4@SiO_2-NH_2$ MNPs have super-paramagnetism and enough saturation magnetization, which can be used as extractants for magnetic solid phase extraction.

3.1.7 Specific surface area analysis. Determine the specific surface area and pore size distribution of the prepared material through nitrogen adsorption and desorption experiments. The nitrogen isotherm adsorption desorption curve shows that
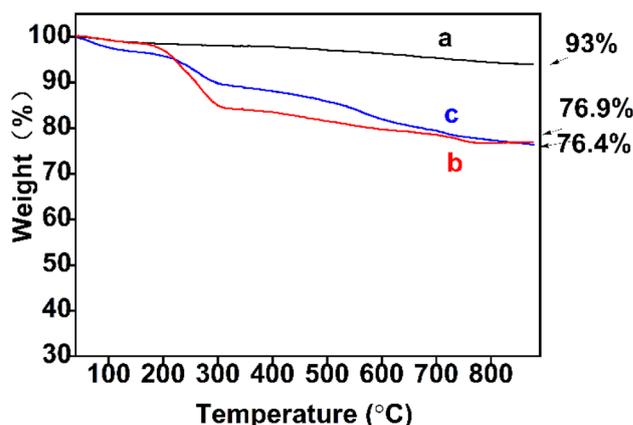

Fig. 9 TGA spectra of (a) $CoFe_2O_4$, (b) $CoFe_2O_4@SiO_2$ and (c) $CoFe_2O_4@SiO_2-NH_2$.

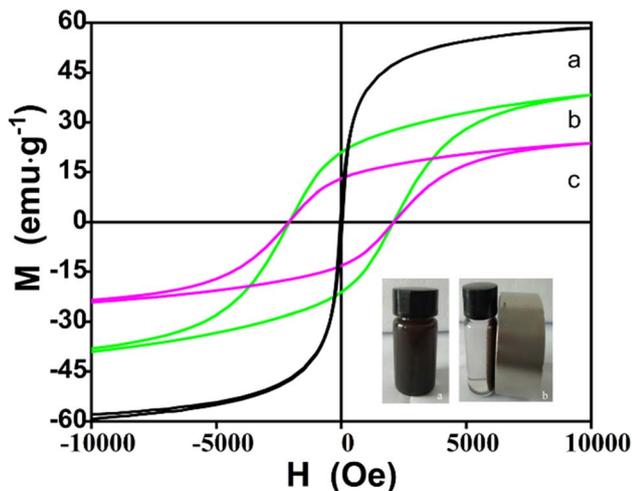Fig. 10 Magnetization at 10 K as a function of magnetic field for (a) $CoFe_2O_4$, (b) $CoFe_2O_4$ @SiO_2 and (c) $CoFe_2O_4$ @SiO_2–NH_2, respectively.

Fig. 11 Extraction efficiency of $CoFe_2O_4$@SiO_2–NH_2 on different heavy metal ions.

these temperature lines belong to type IV in the IUPAC classification. A typical H1 hysteresis loop (Fig. S1†) is observed, indicating that the material is mesoporous, with relatively narrow pore size distribution and uniform spherical size, which is consistent with the observation results of electron microscope. The average pore size of obtained $CoFe_2O_4$@SiO_2–NH_2 is 4.08 nm and the specific surface area of which calculated by BET method is 138.4 m^2 g^{-1}, which thereby increase the lead loading diagram and a larger specific surface area can increase the active surface area.

3.2 Extraction efficiency on different heavy metal ions

The extraction effect of $CoFe_2O_4$@SiO_2–NH_2 on different heavy metal ions was found that, $CoFe_2O_4$@SiO_2–NH_2 has certain extraction ability for various heavy metal ions. The extraction effect is in the order of Pb > Se > Cr > Cd > Hg > Ag, while gold ions are hardly extracted because of the $[AuCl_4]^-$ anionic form in solution (Fig. 11). The intermolecular interactions between functional groups and heavy metals are complex, and the experimental results show that the prepared $CoFe_2O_4$@SiO_2–NH_2 composites have a large difference in the extraction ability of different metal ions and the forms of the extracted lead ions in solution will be further explored by pH and zeta experiments. The results of this experiment suggest that the high affinity of cations for the functional groups of the nanoparticles makes the nanoparticles highly selective.

3.3 Optimizations of lead(ii) extraction

This study found that the selection of extractant, pH value, ionic strength, extraction temperature, extraction time, amount of extractant and other factors had a certain impact on the extraction of metal ions.

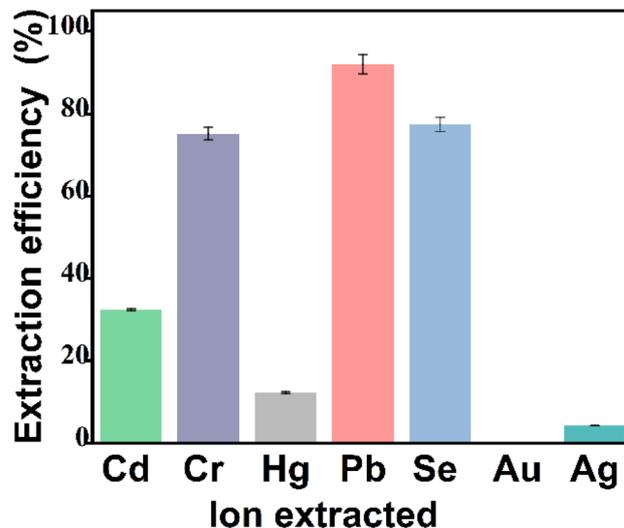Studying the impact of pH within the range of 5.0 to 9.0 on the extraction performance for Pb^{2+}. All pH values were measured by a pH meter (PHS-25B). Lead ion morphology varies with pH value. When pH < 7.0, lead ions mainly exists in the form of free ions and when pH ≥ 7.0, the extraction rate suddenly increases, reaching its maximum at pH 8.0, while the extraction rate sharply decreases when pH > 8.0. Therefore, pH = 8.0 was chosen as the optimal extraction pH (Fig. S2a†). Lead ions gradually exists as $Pb(OH)^+$ and $Pb(OH)_2$ t in the range of pH = 8–11. At pH = 8, the main form of lead present in solution is the positively charged $Pb(OH)^+$ and lead present is $Pb(OH)_2$ at pH > 9, which form is unable to generate coulombic forces with the negative charges on the surface of the extracted material.

Using sodium chloride as the model electrolyte, evaluate the effect of ionic strength in the concentration range of 0–1.0% (w/v) (Fig. S2b†). As the concentration of NaCl increases, the extraction efficiency of Pb^{2+} gradually decreases, mainly due to the competitive extraction of Na^+ caused by the increase in NaCl concentration, resulting in a decrease in extraction efficiency. Based on this result, no electrolyte was added during the extraction process.

Studying the effect of extraction time on extraction rate (Fig. S2c†). The results showed that after 30 minutes of extraction, the extraction equilibrium can be reached, and the extraction rate is greater than 90%. Therefore, the optimal shaking time selected was 30 minutes.

Studying the effect of solution temperature on extraction rate (Fig. S2d†). The results showed that, the extraction rate showed a slow upward trend as the temperature increased at the range of 20–60 °C. At a temperature of 50 °C, the extraction rate could reach over 95%. Therefore, the optimal extraction temperature selected was 50 °C.

3.4 Extraction capacity

Extraction capacity is defined as the maximum amount of Pb(ii) extracted per gram of $CoFe_2O_4$@SiO_2–NH_2. Under the

optimized conditions, the changes in extraction capacity of $CoFe_2O_4@SiO_2–NH_2$ are shown in Fig. S3† at the range of 1.0–10 μg mL^{-1} Pb^{2+} solution concentration. When Pb^{2+} concentration is 4.0 μg mL^{-1}, the extraction capacity of $CoFe_2O_4@SiO_2–NH_2$ for Pb^{2+} is 74.5 mg g^{-1}, which reaches the maximum value. Therefore, the extraction capacity of $CoFe_2O_4@SiO_2–NH_2$ for Pb^{2+} is 74.5 mg g^{-1}.

3.5 Optimizations of lead(II) elution conditions

The effects of eluent selection, eluent concentration, eluent volume and eluent time on the elution effect were investigated as follows. Under optimal conditions, the effect of the same concentration and volume of hydrochloric acid and nitric acid on the elution process of lead was investigated. It can be seen from Fig. S4† that hydrochloric acid has the best elution effect and the highest elution rate. And then the effect of the concentration of 0.2–3 mol L^{-1} hydrochloric acid eluent on the elution rate of Pb^{2+} was investigated. The results showed that 1 mol L^{-1} hydrochloric acid solution had the highest elution rate (>90%) (Fig. S5a†). The effect of eluent volume on elution efficiency was investigated in the range of 2.0–10.0 mL (0.1 g $CoFe_2O_4@SiO_2–NH_2$ MNPs). The eluent rate of hydrochloric acid was more than 85% in the range of 6–10.0 mL and reached more than 95% in the volume of 8.0 mL, as shown in Fig. S5b.† There is no obvious change in elution efficiency when the temperature ranges from 20 to 60 °C, as shown in Fig. S5c.† Therefore, to improve experimental efficiency, room temperature can be selected as the best elution temperature. The effect of elution time was shown in Fig. S5d.† The elution efficiency was increased to more than 95% as the elution time was 2.5 min. Ultrasonic elution can significantly reduce the elution time, and a 2.5 min of ultrasonic elution can be selected as the best elution time.

3.6 Interference experiment of metal elements

The standard solutions of mixed elements (GSB04-2824-2011 and GSB04-1766-2004) were selected to be added into the target lead ion according to the mass ratio of 1 : 10, 1 : 100, 1 : 1000 for interference ion experiment. The experimental results show that K$^+$, Na$^+$ and Fe^{3+} with 1000 times the mass of Pb^{2+} have no interference on $CoFe_2O_4@SiO_2–NH_2$ extraction of Pb^{2+}. Ca^{2+}, Ba^{2+}, Mg^{2+} with 100 times mass ratio of Pb^{2+} have no interference on the extraction of Pb^{2+}, Co^{2+},

Cu^{2+}, Zn^{2+}, Ag$^+$, Mn^{2+}, Ni^{2+} with 10 times mass ratio of Pb^{2+} had no interference on the extraction results. While Cr^{6+}, Cd^{2+}, Se^{2+} interfered with Pb^{2+} extraction (the error of measurement results is ±5%).

3.7 Optimization of analytical wavelengths and analytical performance

The spectral line wavelengths of different elements have different intensity and interference in the atomic emission spectrometer determination (ICPAES 6300). The wavelength order of lead spectral line is 216.999{455}, 220.353{453} nm, etc. (Fig. 12). In this experiment, 220.353 nm spectral line with the strongest signal and the least interference was selected for analysis ($C_0 = 1.0$ mg L^{-1}) (Fig. 12a). Under optimal conditions, the linear range of Pb^{2+} obtained by this method is 0.0–1.00 × 10^4 μg L^{-1}, and the linear fitting equation is $y = 2268c + 19$ ($R^2 = 0.9999$, c: mg L^{-1}) (Fig. 12c), the detection limit (3σ) is 0.027 μg L^{-1}, and the relative standard deviation (RSD) ranges from 0.19 to 3.2%.

3.8 Cycles

In order to investigate the recycling of the $CoFe_2O_4@SiO_2–NH_2$ nanoparticles, they were washed with 8 mL mol L^{-1} hydrochloric acid twice after each MSPE run, and were then used again. The results showed that the extraction capacity did not decrease significantly (extraction rate >80%) after 5 times of recovery (Fig. 13), indicating that the reusability of $CoFe_2O_4@SiO_2–NH_2$ MNPs is not affected after amination.

3.9 Recovery rate experiment

Standard water sample (GBW08608) and actual water sample, with 1–50 μg L^{-1} Pb^{2+} standard solution as the spiked solution, were used to measure the spiked recovery rate, as shown in Table S1.† The recoveries of Pb^{2+} were 94.6% to 106%, meeting the accuracy requirement (80–120%) (Table S1†).

3.10 Actual sample determination

This method is used to determine trace amounts of Pb^{2+} in local water samples, and the results are shown in Table S2.† The experimental results showed that the lead content in local water was at a low allowable level, the method was simple and rapid, and the results were satisfactory. Compared with other
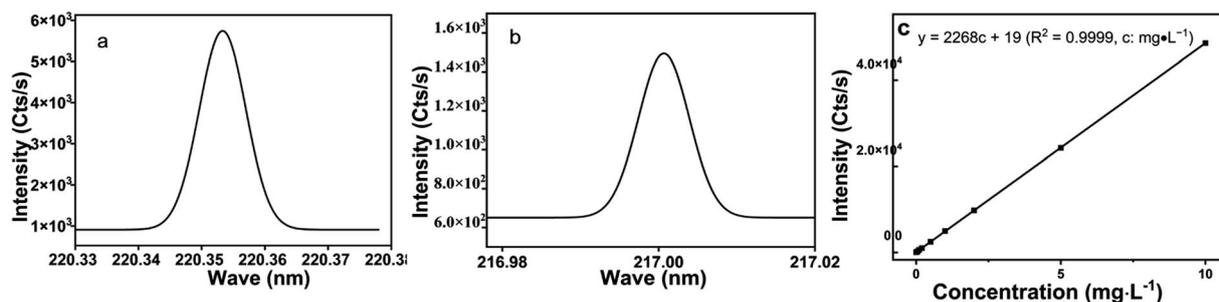

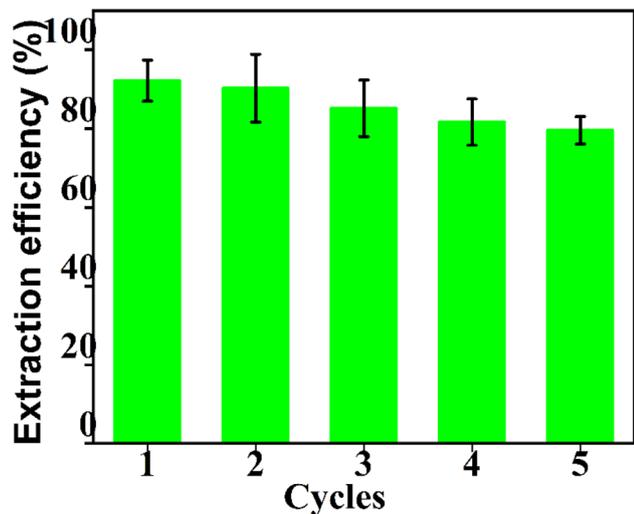**Fig. 12** (a and b) Selection of lead wavelengths, (c) linear fit.

Fig. 13 Cycles of $CoFe_2O_4@SiO_2-NH_2$.

methods for the determination of Pb^{2+} reported in the literature, the results are shown in Table S3,† indicating that this method has the advantages of low detection limit and wide linear range.

3.11 Zeta potential analysis

Zeta potential reflects the type and magnitude of the surface charge of a material.[20] Under different pH values, zeta potential changes of $CoFe_2O_4@SiO_2-NH_2$ MNPs are shown in Fig. S6.† As can be seen from Fig. S6,† the zero-point potential of the MNPs is 5.9. When pH < 5.9 ($pH_{pzc} = 5.9$), $CoFe_2O_4@SiO_2-NH_2$ surface is positively charged. When pH > 5.9, zeta potential is negative, and the ability of the extractant to bind to heavy metals through electrostatic attraction is enhanced at this point.[30] At higher pH, Pb^{2+} hydrolyzed in aqueous solution, resulting in decreased extraction capacity of the MNPs.[21–25]

3.12 Electron binding energy analysis before and after extraction

Element composition and chemical valence state were measured by XPS. The changes of electron binding energy before and after Pb^{2+} extraction by MNPs were compared using XPS high resolution images. The full spectrum of XPS (Fig. S7†) shows the presence of Co, Fe, Si, O, and N elements on $CoFe_2O_4@SiO_2-NH_2$ surface, indicating the successful preparation of $CoFe_2O_4@SiO_2-NH_2$. By comparing the high resolution maps before extraction and after extraction, it can be found that after extraction of Pb^{2+}, the strength of N 1s increases, and the chemical binding energy of N atom moves towards higher binding energy, suggesting that N atom participates in coulomb interaction and N 1s produces a new peak of 406.28 eV (Fig. 14A), which is the result of chelation interaction between the amino group on the extractant and metal ions. By comparing O 1s peaks of before extraction and after extraction (Fig. 14B), it can be seen that O atom moves towards higher

binding energy after extraction, suggesting that O atom participates in coulomb interaction.[21,26]

3.13 Adsorption kinetics experiment

In order to investigate the adsorption kinetics of lead(II) on $CoFe_2O_4@SiO_2-NH_2$, pseudo-first order and pseudo-second order kinetic models were used.

Pseudo-first-order kinetic models formula:

$$\ln(Q_e - Q_t) = \ln Q_e - k_1 t \tag{2-1}$$

Pseudo-second-order kinetic models formula,

$$\frac{1}{Q_t} = \frac{1}{k_2 Q_e^2} \frac{1}{t} + \frac{1}{Q_e} \tag{2-2}$$

$$\ln(q_e - q_t) = \ln q_e - k_1 t \tag{2-3}$$

Q_e: the adsorption amount of lead(II) by $CoFe_2O_4@SiO_2-NH_2$ at equilibrium, $mg\ g^{-1}$. Q_t: the adsorption amount of lead(II) by $CoFe_2O_4@SiO_2-NH_2$ at t time, $mg\ g^{-1}$. t: adsorption time, min; k_1: pseudo-first-order adsorption rate constant, $g\ mg^{-1}\ min^{-1}$. k_2: pseudo-second-order adsorption rate constant, $g\ mg^{-1}\ min^{-1}$.

The value of Q_e and k_1 can be obtained after fitting the graph of t by Q_t and by plotting t by t/Q_t in formula (2-2), Q_e and k_2 can be obtained.

In this experiment, two dynamic models were selected to fit the experimental data, describe the dynamic characteristics of the extraction process, and speculate the rate control steps of the extraction process, including the pseudo-first-order kinetic model (formula (2-1)) and the pseudo-second-order kinetic model (formula (2-2)). The correlation coefficient of the quasi-second-order kinetic model ($R^2 = 0.9999$) is higher than that of the quasi-first-order kinetic model ($R^2 = 0.5625$) (Table S4†). In addition, Q_t (75.8 $mg\ g^{-1}$) of the pseudo-second-order kinetic model is closer to the experimental $Q_{e,exp}$ (74.5 $mg\ g^{-1}$). The adsorption kinetics experiments of $CoFe_2O_4@SiO_2-NH_2$ on Pb(II) show that the adsorption conforms to the pseudo-second-order kinetic model, and the adsorption can be considered as monomolecular chemisorption (Fig. 15). Langmuir model is more suitable to describe the extraction behavior of extractants.

3.14 Adsorption isothermal model

Langmuir (Fig. 16a) and Freundlich (Fig. 16b) adsorption isotherm models were used to study the extraction process of lead ions by $CoFe_2O_4@SiO_2-NH_2$ nanocomposites.

Langmuir adsorption isotherm model is shown in formula (2-4)

$$\frac{C_e}{Q_e} = \frac{1}{Q_{max}}C_e + \frac{1}{Q_{max}K_L} \tag{2-4}$$

Freundlich adsorption isotherm model is shown in formula (2-5)
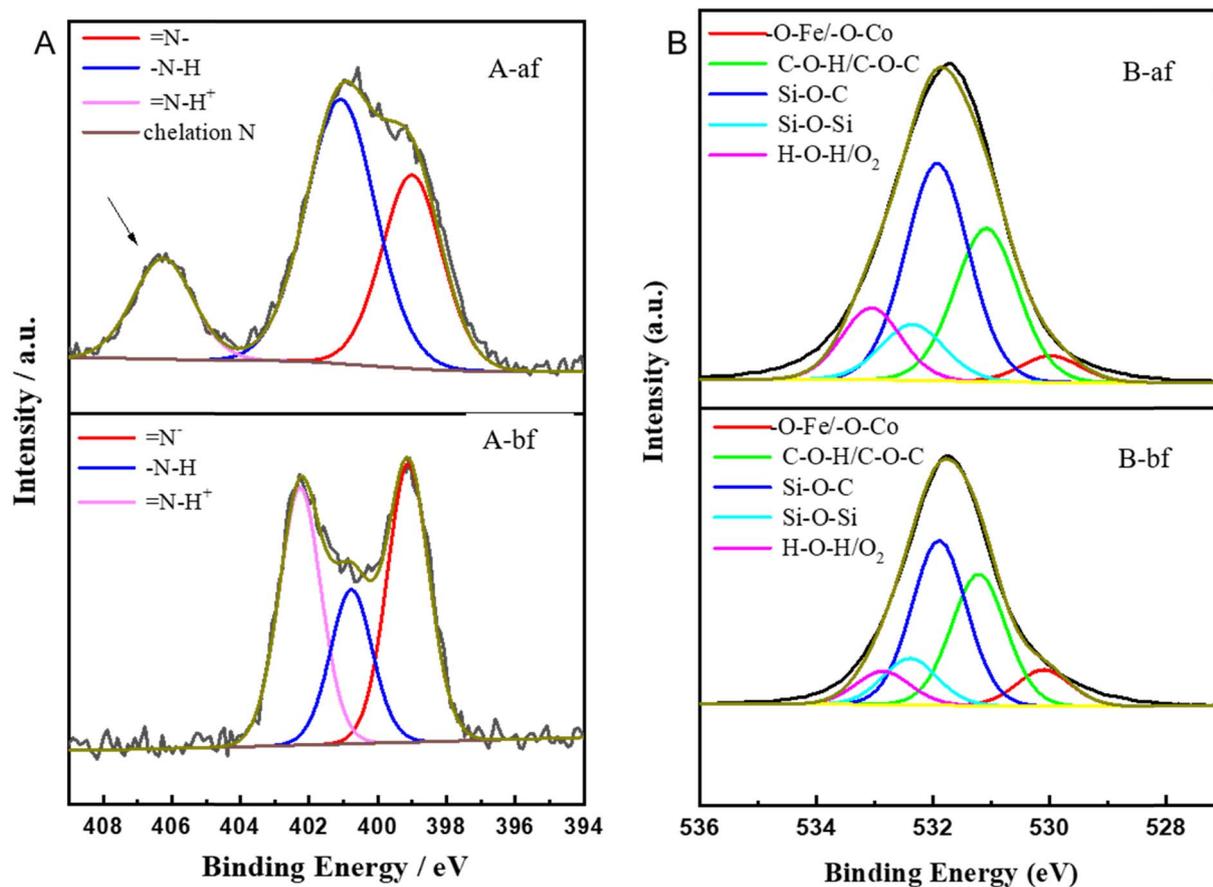
$$\ln Q_e = \frac{1}{n}\ln C_e + \ln K_F \tag{2-5}$$

Fig. 14 XPS core-level spectra of CoFe$_2$O$_4$@SiO$_2$–NH$_2$ of the samples before and after extraction (N 1S (A), O 1S (B)).
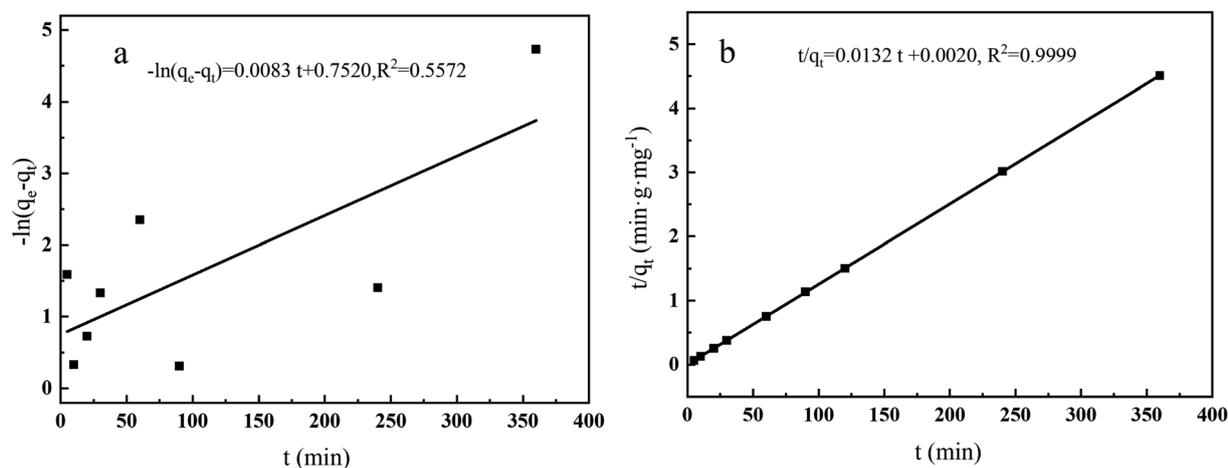

Fig. 15 Effect of kinetic fittings of pseudo-first order (a) and pseudo-second order (b).

In the formula, Q_e: the equilibrium adsorption capacity of the extractant on metal ions, mg g^{-1}; Q_{max}: maximum adsorption capacity of extractant on metal ions, mg g^{-1}; K_L: Langmuir adsorption equilibrium constant, L mg^{-1}; C_e: the equilibrium concentration of metal ions in the solution, mg L^{-1}; $1/n$ and K_F are Freundlich characteristic constants, representing adsorption capacity and strength, respectively. As can be seen from the figure, the correlation coefficient of Langmuir adsorption isotherm ($R^2 = 0.9867$) is higher than that of Freundlich adsorption isotherm ($R^2 = 0.7847$) (Table S5†). This indicates that Langmuir model is more suitable to describe the extraction process than Freundlich model.
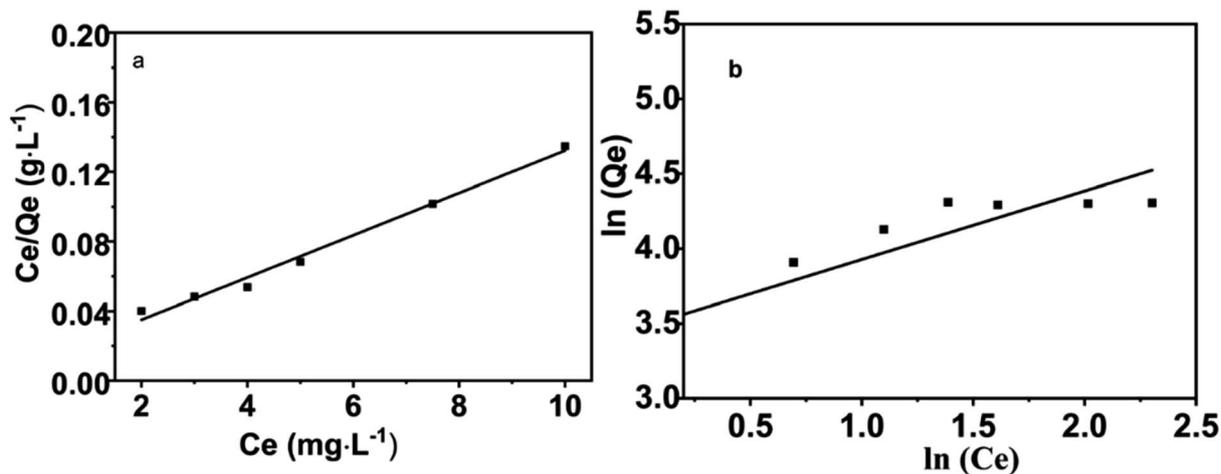
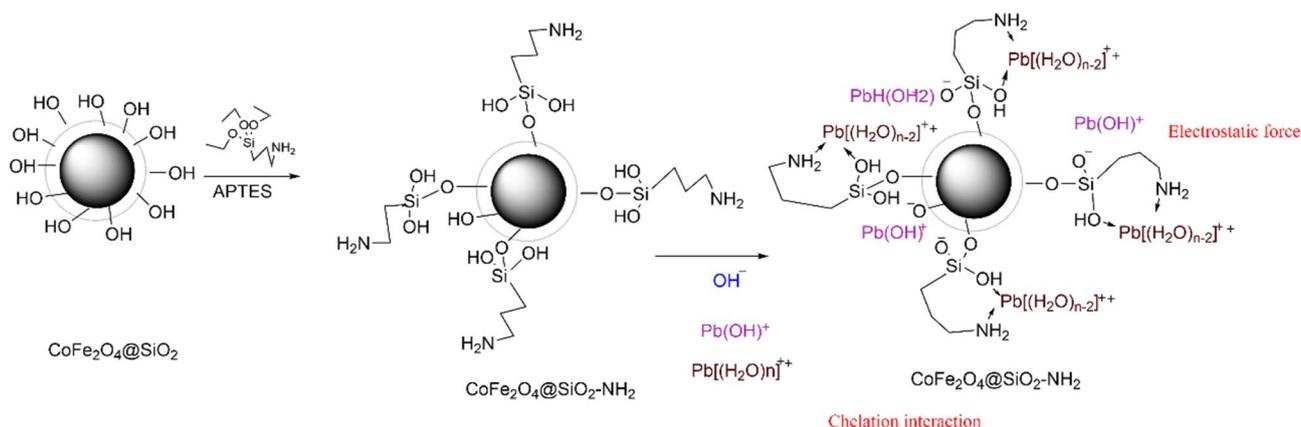**Fig. 16** Langmuir (a) and Freundlich (b) adsorption isotherm.

Fig. 17 The main adsorption mechanism of $CoFe_2O_4@SiO_2-NH_2$ to lead ions.

4   Conclusion

$CoFe_2O_4@SiO_2-NH_2$ MNPs with a core–shell structure were successfully prepared *via* a mild and facile hydrothermal method in the presence of water. The saturation magnetization of the as-prepared material was 24.2 emu g^{-1}, which means a good magnetic separation performance. The Langmuir adsorption capacity of Pb^{2+} was 74.5 mg g^{-1} at 323 K and a pH of 8, and the MNPs could be recycled for 5 times. pH plays an important role in metal ion extraction. The pH value affects the interaction between the extractant and the target ion during the extraction process by affecting the morphology of Pb^{2+} in the aqueous solution and the surface charge of the extractant.[27] At pH = 8, lead ions mainly exist in the form of $Pb(OH)^+$ in the solution while as pH increases, lead ions coexist in the form of $Pb(OH)^+$ and $Pb(OH)_2$. When pH = 11, the form of lead ions mainly exists in $Pb(OH)_2$, so an excessively high pH value will lead to a decrease in the extraction capacity of lead ions.[21–25] Besides, zeta potential of the MNPs was negative when pH > 5.9, and the ability of the extractant to bind to heavy metals through electrostatic attraction was enhanced at this point.[28] Physical

adsorption of adsorbents is strongly influenced by the pore size distribution and surface area of the adsorbent.[29] An increase in micropores increases the specific surface area and further promotes physical adsorption, whereas an increase in meso-pores promotes the diffusion of adsorbate to accelerate the adsorption kinetics.[30] The prepared MNPs has micropores and mesopores, and the BET experiments show that there is a weak force of physical adsorption. The XPS experiments show that the chemical binding energy of O and N changes after extraction, suggesting that the carboxyl, hydroxyl, and amine groups on the $CoFe_2O_4@SiO_2-NH_2$ interact with the lead ions by surface complexation. A large number of hydroxyl-activated groups are present on the surface of the SiO_2, and the SiO_2 coats the $CoFe_2O_4$, which forms the shell–core structure and increases the surface complexation of the pure $CoFe_2O_4$. A large number of hydroxyl groups existed on the surface of SiO_2, and SiO_2 coated $CoFe_2O_4$, forming a shell–core structure, which increased the stability, dispersion, and adsorption of pure $CoFe_2O_4$, nanoparticles in solution. A large number of hydroxyl groups existed on the surface of SiO_2 grafted silanol groups on one end of the APTES through covalent bonding. The silanol on

the APTES were bonded with each other to form a gel reticulation structure in order to increase the extraction ability of the metal ions. Amino groups on the other end of the APTES increased the amino group at the other end of APTES increases the selective extraction ability of the target ions and causes an increase in the surface charge of the prepared material, which increases the dispersion of the material in aqueous solution, the electrostatic attraction with the target ions, and the interaction force between the surface N atoms and the target ions. The main adsorption mechanism of $CoFe_2O_4@SiO_2–NH_2$ to lead ions was the binding of amino groups and silicon hydroxyl intermediates from APTES with lead ions to form a chelation interaction, coulombic interactions between electronegative O atoms from silicon hydroxyl and $Pb(OH)^+$, as well as the electrostatic attraction between the negative charge O atoms in the surface of $CoFe_2O_4@SiO_2–NH_2$ and lead cations, so as to achieve the purpose of removing lead ions from the solution (Fig. 17). Thus, the synthesized magnetic nanocomposites can be used in many industries for the removal of contaminated metal ions, which is beneficial in achieving sustainable development.

Conflicts of interest

There are no conflicts to declare.

Acknowledgements

References

1 S. Zhang, H. Niu, et al., Arsenite and arsenate adsorption on coprecipitated bimetal oxide magnetic nanomaterials: $MnFe_2O_4$ and $CoFe_2O_4$, Chem. Eng. J., 2010, 158(3), 599–607.

2 V. H. Ojha and K. M. Kant, Investigation of structural and magnetic properties of strained $CoFe_2O_4$ nanoparticles, J. Phys. Chem. Solids, 2021, 148, 109655.

3 X. Wu, W. Wang, et al., PEG-assisted hydrothermal synthesis of $CoFe_2O_4$ nanoparticles with enhanced selective adsorption properties for different dyes, Appl. Surf. Sci., 2016, 389, 1003–1011.

4 P. Arévalo-Cid, J. Isasi, et al., Comparative study of core-shell nanostructures based on amino-functionalized $Fe_3O_4@SiO_2$ and $CoFe_2O_4@SiO_2$ nanocomposites, J. Alloys Compd., 2018, 766, 609–618.

5 A. F. P. Allwin Mabes Raj, M. Bauman, et al., Superparamagnetic Spinel-Ferrite Nano-Adsorbents Adapted for Hg^{2+}, Dy^{3+}, Tb^{3+} Removal/Recycling: Synthesis, Characterization, and Assessment of Toxicity, Int. J. Mol. Sci., 2023, 24(12), 10072.

6 W. Wu, Q. He, et al., Magnetic iron oxide nanoparticles: Synthesis and surface functionalization strategies, Nanoscale Res. Lett., 2008, 3(11), 397–415.

7 C. Ren, X. Ding, et al., Core–shell superparamagnetic monodisperse nanospheres based on amino-functionalized $CoFe_2O_4@SiO_2$ for removal of heavy metals from aqueous solutions, RSC Adv., 2017, 7(12), 6911–6921.

8 S. V. Thakkar and L. Malfatti, Silica-graphene porous nanocomposites for environmental remediation: A critical review, J. Environ. Manage., 2021, 278(P1), 111519.

9 Y. Wang, R. Zhou, et al., Novel environmental-friendly nanocomposite magnetic attapulgite functionalized by chitosan and EDTA for cadmium (II) removal, J. Alloys Compd., 2020, 817, 153286.

10 L. Mueller, H. Traub, et al., Trends in single-cell analysis by use of ICP-MS, Anal. Bioanal. Chem., 2014, 406, 6963–6977.

11 A. F. Werner Stober, Department. Controlled Growth of Monodisperse Silica Spheres in the Micron Size Range 1 WERNER, J. Colloid Interface Sci., 1968, 26(1968), 62–69.

12 H. Wang, J. Huang, et al., A facile synthesis of monodisperse $CoFe_2O_4/SiO_2$ nanoparticles, Appl. Surf. Sci., 2011, 257(16), 7107–7112.

13 X. Wang, Z. Zhang, et al., A Mild and Facile Synthesis of Amino Functionalized $CoFe_2O_4@SiO_2$ for Hg(II) Removal, Nanomater, 2018, 8(9), 673.

14 Standardization Administration of PRC (SAC), GB/T 14848-2017 Groundwater Quality Standards, Published online, 2017, pp. 1–19.

15 H. Wang, J. Huang, et al., A facile synthesis of monodisperse $CoFe_2O_4/SiO_2$ nanoparticles, Appl. Surf. Sci., 2011, 257(16), 7107–7112.

16 B. Tang, L. Luan, et al., Removal of aqueous Cd(II) and Ni(II) by aminopyridine functionalized magnetic Fe_3O_4 nanocomposites, J. Mol. Liq., 2021, 331, 115780.

17 C. Ren, X. Ding, et al., Core-shell superparamagnetic monodisperse nanospheres based on amino-functionalized $CoFe_2O_4@SiO_2$ for removal of heavy metals from aqueous solutions, RSC Adv., 2017, 7(12), 6911–6921.

18 H. Zhang, H. Li, et al., Synthesis of Magnetic CoFe 2 O 4 Nanoparticles and Their Efficient Degradation of Diclofenac by Activating Persulfate via Formation of Sulfate Radicals, J. Nanosci. Nanotechnol., 2018, 18(10), 6942–6948.

19 C. R. Ren, X. G. Ding, et al., Core-shell superparamagnetic monodisperse nanospheres based on amino-functionalized $CoFe_2O_4@SiO_2$ for removal of heavy metals from aqueous solutions, RSC Adv., 2017, 7(12), 6911–6921.

20 D. C. Culita, C. M. Simonescu, et al., o-Vanillin functionalized mesoporous silica – coated magnetite nanoparticles for efficient removal of Pb(II) from water, J. Solid State Chem., 2016, 238, 311–320.

21 S. P. Kuang, Z. Z. Wang, *et al.*, Preparation of triethylene-tetramine grafted magnetic chitosan for adsorption of Pb(II) ion from aqueous solutions, *J. Hazard. Mater.*, 2013, **260**, 210–219.

22 M. Zhong, H. Kou, *et al.*, Nasal Delivery of D-Penicillamine Hydrogel Upregulates a Disintegrin and Metalloprotease 10 Expression via Melatonin Receptor 1 in Alzheimer's Disease Models, *Front. Aging Neurosci.*, 2021, **13**, 660249.

23 S. Zhuang, K. Zhu, *et al.*, Fibrous chitosan/cellulose composite as an efficient adsorbent for Co(II) removal, *J. Cleaner Prod.*, 2021, **285**, 124911.

24 J. Cao, P. Wu, *et al.*, Ultrafast Fabrication of Self-Healing and Injectable Carboxymethyl Chitosan Hydrogel Dressing for Wound Healing, *ACS Appl. Mater. Interfaces*, 2021, **13**(20), 24095–24105.

25 J. R. Evans, W. G. Davids, *et al.*, Kinetics of cadmium uptake by chitosan-based crab shells, *Water Res.*, 2002, **36**(13), 3219–3226.

26 H. K. An, B. Y. Park, *et al.*, Crab shell for the removal of heavy metals from aqueous solution, *Water Res.*, 2001, **35**(15), 3551–3556.

27 M. Kumari, C. U. Pittman, *et al.*, Heavy metals [chromium (VI) and lead (II)] removal from water using mesoporous magnetite (Fe_3O_4) nanospheres, *J. Colloid Interface Sci.*, 2015, **442**(Vi), 120–132.

28 C. Santhosh, E. Daneshvar, *et al.*, Magnetic SiO_2@$CoFe_2O_4$ nanoparticles decorated on graphene oxide as efficient adsorbents for the removal of anionic pollutants from water, *Chem. Eng. J.*, 2017, **322**, 472–487.

29 C. Santhosh, V. Velmurugan, *et al.*, Role of nanomaterials in water treatment applications: A review, *Chem. Eng. J.*, 2016, **306**, 1116–1137.

30 L. Li, Y. Lv, *et al.*, Enhance pore structure of cyanobacteria-based porous carbon by polypropylene to improve adsorption capacity of methylene blue, *Bioresour. Technol.*, 2022, **343**(2021), 126101.